Research article

Electronic metal-support interactions for defect-induced Ru/Co-Sm$_2$O$_3$ mesosphere to achieve efficient NaBH$_4$ hydrolysis activity

Shuqing Zhou [a], Qiuling Yang [a], Yi Liu [a], Lianrui Cheng [a], Tayirjan Taylor Isimjan [b,*], Jianniao Tian [a,*], Xiulin Yang [a,*]

[a] Guangxi Key Laboratory of Low Carbon Energy Materials, School of Chemistry and Pharmaceutical Sciences, Guangxi Normal University, Guilin 541004, China
[b] Saudi Arabia Basic Industries Corporation (SABIC) at King Abdullah University of Science and Technology (KAUST), Thuwal 23955-6900, Saudi Arabia

ABSTRACT

Crafting resilient catalysts that promote H$_2$ production through the hydrolysis of hydrogen storage materials like sodium borohydride stands paramount for the impending hydrogen economy. In this study, we propose a versatile metal–organic framework (MOF)-assisted approach to systematically explore the impact of electron-metal support interaction (EMSI) of Ru-modified Co-Sm$_2$O$_3$ (Ru/Co-Sm$_2$O$_3$) on H$_2$ evolution from NaBH$_4$ hydrolysis. Strategic annealing at 800 °C induces cobalt vacancies on the Ru/Co-Sm$_2$O$_3$ surface, optimizing the exposure of active sites and amplifying mass-charge transfer efficiency. Consequently, the defect-enriched Ru/Co-Sm$_2$O$_3$ showcases an impressive hydrogen generation rate (HGR = 0.430 mol min^{-1} g$_{catalyst}^{-1}$) and outstanding cycling resilience, eclipsing the performance of most contemporary catalysts. Experimental findings reveal that Sm can not only adjust the Ru lattice spacing to accommodate more BH$_4^-$, but also modulate the Co vacancy concentration, thus bolstering the charge transport and ameliorating the catalyst's electrical conductivity. DFT calculations confirm that the Michaelis-Menten/Eley-Rideal mechanism is more appropriate to explain the hydrolysis of NaBH$_4$.

1. Introduction

Declining fossil fuel reserves, coupled with the environmental challenges of burning them, highlight the urgent need to explore sustainable and clean energy alternatives [1]. In this context, hydrogen has garnered significant interest due to its impressive energy density and high heat of combustion [2]. Of the diversified methods for hydrogen production, the hydrolysis of NaBH$_4$ has emerged as one of the predominant techniques, attributed to its high hydrogen storage content (10.6 wt%), stability in alkaline solutions, the purity of the hydrogen produced, and its nontoxic nature [3,4]. Intriguing, the by-products of NaBH$_4$ hydrolysis can be regenerated using cost-effective materials and a rapid ball milling method [5], paving the way for potential applications in sustainable energy advancement. Nevertheless, challenges such as the slow kinetics of NaBH$_4$ hydrolysis and suboptimal hydrogen yields need to be addressed before large-scale commercialization [6,7].

Although platinum-based catalysts show exceptional performance in sodium borohydride hydrolysis, their broad-scale utilization is constrained by their limited availability and high cost [8,9]. Conversely, Ru-based catalysts, from the same metal family as Pt, also offer commendable performance at just a third of the price and are more abundant [10]. Yet, the efficacy of singular Ru catalysts remains suboptimal. One approach to bolster the performance of Ru-based catalysts is through the metal-support effect, leveraging the resultant electron metal-support interaction (EMSI). This interaction can adeptly manipulate the electronic structure and boost the catalytic efficiency of the loaded metal nanoparticles [11]. As an illustration, Tuan et al. utilized EMSI engineering to anchor Ru nanoparticles onto octahedral ZIF-67, resulting in notable activity in NaBH$_4$ hydrolysis [12]. Metal-organic frameworks (MOFs), with their expansive surface areas and adaptable morphologies, present distinct advantages [13]. Their diverse metal nodes/organic ligands, along with their meticulously organized porous structure, endows MOFs with a plethora of coordination sites. This structure facilitates the induction of surface defects during annealing, subsequently enhancing electron transfer and elevating catalytic performance [14]. As a case in point, our team developed a Ru-decorated MOF-derived CoO$_x$@NPC core–shell structure that showcased exemplary NaBH$_4$ hydrolysis activity [15]. Moreover, introducing vacancies

represent a valid strategy to fine-tune the electronic structure and charge carrier concentration in the catalyst, leading to heightened catalytic activity [16]. The viability of this defect engineering approach was affirmed through the creation of efficient NaBH$_4$ hydrolysis catalysts enriched with phosphorus and oxygen vacancies in our prior work [17,18]. Further research indicates that expanding lattice spacing by doping with other atoms can create more storage space for reactants, augmenting the catalyst's electrical conductivity and enhancing transport and rate attributes [19].

Combining the aforementioned insights, we engineered the Ru-loaded Sm-doped Co spheres using a defect engineering approach, resulting in a highly efficient catalyst named Ru/Co-Sm$_2$O$_3$. And then rigorously assessed its efficacy in NaBH$_4$ hydrolysis. The catalyst's intricate microsphere structure and ample cobalt vacancy led the Ru$_{4.7}$/Co-Sm$_2$O$_3$ to achieve an ultra-high hydrogen generation rate (HGR = 0.430 mol min^{-1} g$^{-1}_{catalyst}$) and brilliant reusability in alkaline NaBH$_4$ hydrolysis, surpassing many noble metal catalysts documented in existing literature. The UPS and XPS results showcased that the defect-induced EMSI contributed to a significant charge redistribution between the charge carriers of Ru and Co-Sm$_2$O$_3$, which promoted charge transport and improved the activity of the catalysts. Density functional theory (DFT) calculations exhibited that the binding energy of the Michaelis-Menten/Eley-Rideal mechanism (0.71 eV) for the rate-determining step was significantly lower than that of the Langmuir-Hinshelwood mechanism (1.88 eV), confirming that the Michaelis-Menten/Eley-Rideal mechanism was the optimal mechanism for the hydrolysis reaction of NaBH$_4$. This research is poised to significantly impact the methods of producing superior catalysts, emphasizing lattice extensibility through defect engineering strategies.

2. Experimental section

2.1. Materials

Cobalt(II) nitrate hexahydrate (Co(NO$_3$)$_2$·6H$_2$O ≥ 99 %, Aladdin), Sodium hydroxide (NaOH ≥ 96.0 %, Xilong Science), Samarium(III) nitrate hexahydrate (Sm(NO$_3$)$_3$·6H$_2$O ≥ 99.9 %, Aladdin), Ammonia borane (NH$_3$·BH$_3$ ≥ 97.0 %, Aladdin), Sodium borohydride (NaBH$_4$ ≥ 98.0 %, Sinopharm Group), Polyvinyl pyrrolidone ((C$_6$H$_9$NO)$_n$, PVP, Aladdin), N,N-Dimethylformamide (DMF) and Trimesic acid-1,3,5-Benzenetricarboxylic acid (C$_9$H$_6$O$_6$ (H$_3$BTC) ≥ 98 %, Aladdin). All chemicals were of analytical grade and did not require further purification. All aqueous solutions were prepared with deionized water.

2.2. Synthesis of CoSm-BTC

Initially, 0.845 g Co(NO$_3$)$_2$·6H$_2$O, 0.043 g Sm(NO$_3$)$_3$·6H$_2$O and 0.120 g PVP were dissolved in 30 ml DMF. This solution was sonicated for 15 min, and then 15 ml of DMF (containing 0.630 g of H$_3$BTC) was added dropwise. Stirring continued for an additional 30 min, the mixture was transferred to a 100 ml Teflon-lined reactor and held at 160 °C for 24 h. After cooling to room temperature, the product was centrifuged, washed thrice with DMF, and dried in a 60 °C oven overnight to produce CoSm-BTC. Variants with different molar ratios (Co: Sm = 1: 1, 10: 1, 20: 1, and 40: 1) were labeled CoSm-BTC-1, CoSm-BTC-2, CoSm-BTC-3, and CoSm-BTC-4, respectively, and were synthesized using the identical procedure.

2.3. Synthesis of Co-Sm$_2$O$_3$

A predetermined quantity of CoSm-BTC was placed in a quartz boat and heated to 800 °C (alternatively, 700 or 900 °C) at a rate of 5 °C/min in an argon atmosphere. After maintaining this temperature for 3 h, the system was allowed to cool naturally to yield the black Co-Sm$_2$O$_3$ powder.

2.4. Synthesis of Ru/Co-Sm$_2$O$_3$

Specifically, 50 mg of Co-Sm$_2$O$_3$ was weighed and dispersed in 40 mL of H$_2$O, while 9 mg (3, 6, 12 and 15 mg) of RuCl$_3$ was added and sonicated for 15 min, followed by stirring of the solution for 4 h at room temperature. Then 5 mL of NH$_3$·BH$_3$ solution (0.13 M) was added dropwise to the solution and stirring was continued for 30 min. After centrifuging to collect the catalysts, wash it three times with deionized water and ethanol, and then dry it under vacuum at 60 °C for 12 h to obtain the Ru$_{4.7}$/Co-Sm$_2$O$_3$ (Ru$_{2.4}$/Co-Sm$_2$O$_3$, Ru$_{3.7}$/Co-Sm$_2$O$_3$, Ru$_{5.6}$/Co-Sm$_2$O$_3$ and Ru$_{7.1}$/Co-Sm$_2$O$_3$,) catalysts. As mentioned above, different supports for Ru$_{4.7}$/Co and Ru$_{4.7}$/Sm$_2$O$_3$ catalysts were experimentally prepared.

3. Results and discussion

3.1. Synthesis strategy and microstructure analysis

Creating a microspherical structure in Ru/Co-Sm$_2$O$_3$ catalysts necessitates the precise application of vacancy engineering. Hence, we implemented a MOF-mediated pyrolysis-reduction strategy to realize this goal. Fig. 1a schematically displayed the fabrication process of Ru/Co-Sm$_2$O$_3$ spherical structure (see Experimental Section for details). Firstly, porous CoSm-BTC spheres were synthesized using a straightforward hydrothermal technique, as shown in Fig. S1a. The CoSm-BTC precursor was then pyrolyzed, resulting in a Co-Sm$_2$O$_3$ hybrid featuring a textured surface (Fig. S1b). In the final step, the Ru precursor was integrated into the Co-Sm$_2$O$_3$ through an impregnation reduction method, yielding the Ru/Co-Sm$_2$O$_3$ catalysts (Fig. 1b). Impressively, the surface of the microsphere was populated with derivative nanoparticles culminating in a hierarchical micro/nanostructure. This design underscores the effectiveness of our methodology in securing nanoparticles uniformly [20]. This distinctive micro/nanoarchitecture maximizes the electrochemical surface area, making it readily accessible [21]. As projected, the Co and Sm elements within the carbonized MOF transitioned into a Co-Sm$_2$O$_3$ heterojunction framework. Meanwhile, Ru^{3+} was reduced by amino borane to produce metal Ru-modified Ru/Co-Sm$_2$O$_3$, with the resultant Ru content measuring at 4.7 wt% as confirmed by ICP-AES analyses (Table S6).

The internal morphological structure of Ru$_{4.7}$/Co-Sm$_2$O$_3$ hybrid was tracked by Transmission electron microscopy (TEM) (Fig. S2). Fig. 1c illustrates the uniform dispersion of Ru nanoparticles on the Co-Sm$_2$O$_3$ surface, with an average particle size of approximately 15.4 nm. This size is smaller than that of Ru$_{4.7}$/Co (24.3 nm) and Ru$_{4.7}$/Sm$_2$O$_3$ (22.1 nm, Fig. S3). Notably, a smaller particle size typically presented more active sites, enhancing activity. High-resolution TEM (HR-TEM) images of the Ru$_{4.7}$/Co-Sm$_2$O$_3$ catalyst revealed the presence of Ru, Co, and Sm$_2$O$_3$ phases on the microspherical surface. The lattice spacings of 2.04, 2.43, and 3.10 Å corresponded to the Co (1 1 1), Ru (1 0 0), and Sm$_2$O$_3$ (2 2 2) crystal planes, respectively, as shown in Fig. 1d [22–24]. Concurrently, the Ru (1 0 0) lattice spacings for Ru$_{4.7}$/Sm$_2$O$_3$ and Ru$_{4.7}$/Co are 2.56 and 2.28 Å, respectively, as depicted in Fig. 1e-f. Notably, the Ru (1 0 0) lattice spacing in Ru$_{4.7}$/Co-Sm$_2$O$_3$ fell between 2.56 and 2.28 Å. This suggests that Sm doping effectively modulates the lattice expansion of Ru, creating optimal adsorption/desorption channels for reactants and enhancing reaction kinetics [19]. The high-angle annular dark-field scanning TEM (HAADF-STEM), along with the corresponding elemental mapping (shown in Fig. 1g), indicated that while Co is at the core of the microsphere, Sm and Ru elements were uniformly spread across the entire surface structure. Intriguingly, Sm interacted closely with Ru on the sphere's surface, influencing the Ru lattice and revealing more active sites. This interaction substantially enhances the catalyst's inherent activity [9].
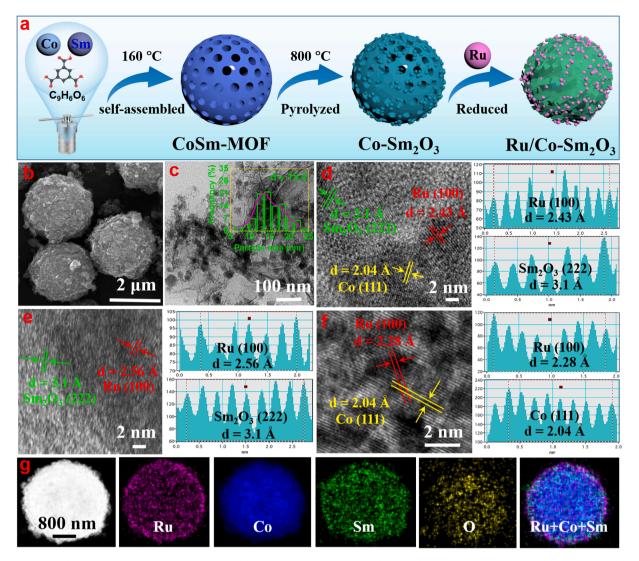
Fig. 1. (a) Schematic diagram of the synthesis of Ru/Co-Sm$_2$O$_3$. (b) SEM image, (c) TEM image (the inset depicted the particle size distribution of Ru particles) of Ru/Co-Sm$_2$O$_3$. High-resolution (HR)-TEM images of (d) Ru$_{4.7}$/Co-Sm$_2$O$_3$, (e) Ru$_{4.7}$/Sm$_2$O$_3$ and (f) Ru$_{4.7}$/Co, as well as the intensity profile of corresponding areas. (g) HAADF-STEM image and elemental mappings (Ru, Co, Sm and O) of Ru$_{4.7}$/Co-Sm$_2$O$_3$.

3.2. Crystallinity, porosity and defect analysis

The crystalline properties of the catalysts were assessed using powder X-ray diffraction (XRD) spectra. As depicted in Fig. S4a, increasing the Co content led to a weakened diffraction peak intensity of Sm-MOF. Post high-temperature calcination, CoSm-MOF transitioned into Co (JCPDS: 89–4307) and Sm$_2$O$_3$ (JCPDS: 42–1461) as shown in Fig. S4b [25]. Notably, the Sm$_2$O$_3$ diffraction peak at 28.2° diminished with rising Co content, confirming the emergence of the Co-Sm$_2$O$_3$ heterogeneous structure. However, after integrating Ru nanoparticles into Co-Sm$_2$O$_3$, no distinct diffraction peaks were discernible, likely due to the amorphous state or minimal Ru content (Fig. 2a) [12]. The Raman spectrum showcased broad D (~1375 cm^{-1}) and G (~1589 cm^{-1}) carbon bands, corresponding to defective/disordered and graphitic carbon, respectively [26].Typically, the intensity ratio between D and G bands (I_D/I_G) was applied to evaluate the level of defects in nanomaterials [27]. In Fig. 2b, the I_D/I_G values of Ru$_{4.7}$/Sm$_2$O$_3$, Ru$_{4.7}$/Co and Ru$_{4.7}$/Co-Sm$_2$O$_3$ were 0.71, 1.12, and 1.04, respectively. Higher I_D/I_G intensity ratio of Ru$_{4.7}$/Co-Sm$_2$O$_3$ manifested the existence of structural defects, which favored to adjust the electronic structure of the metal and neighboring C atoms and bring in diversified active sites, thus boosting the catalytic performance [28,29]. Electron paramagnetic resonance (EPR) further confirmed cobalt

vacancy presence in various samples (Fig. S5). Visibly, Co and Co-Sm$_2$O$_3$ acquired a nearly symmetric EPR signal around g = 2.05, while Sm$_2$O$_3$ did not, demonstrating the existence of cobalt vacancy that captured unpaired electrons [30]. Interestingly, the intensity of the cobalt vacancy decreased with added Sm, pointing to significant electronic interaction between Co and Sm$_2$O$_3$ [27]. Introducing Ru to the support largely maintained defect levels, suggesting Ru had minimal impact on Co defects, while Sm played a regulatory role (Fig. 2c) [31]. The rich cobalt vacancies and associated unpaired electrons in Ru$_{4.7}$/Co-Sm$_2$O$_3$ substantially tuned the local electronic structure and orbital coupling, facilitating to expose more active sites, which can optimize the adsorption capacity of active intermediates [32]. Examination of N$_2$ adsorption–desorption isotherms revealed that Ru$_{4.7}$/Co-Sm$_2$O$_3$ exhibited typical type IV curves with H3 hysteresis loops, indicative of mesoporosity (Fig. 2d) [28]. Such mesopores act as separators, inhibiting Ru nanoparticle agglomeration and enhancing active site accessibility [33]. According to the Brunauer-Emmett-Teller (BET) analysis, the specific surface area of Ru$_{4.7}$/Co-Sm$_2$O$_3$ was calculated to be 101.7 m^2 g^{-1} with a pore size distribution of 15.1 nm.

3.3. XPS and UPS analysis

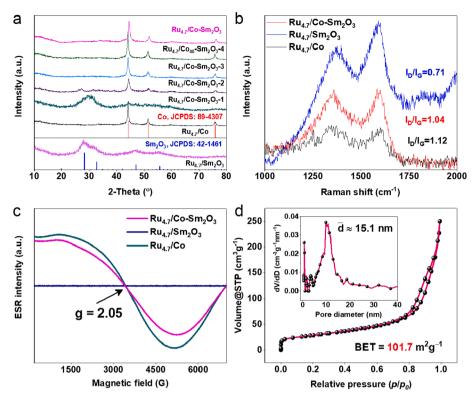Depth profile X-ray photoelectron spectroscopy (XPS) was employed

Fig. 2. (a) XRD patterns, (b) Raman spectra, and (c) electron paramagnetic resonance (EPR) spectra of the different catalysts. (d) Nitrogen adsorption–desorption isotherms and corresponding pore size distribution of $Ru_{4.7}/Co-Sm_2O_3$.

to elucidate the surface chemical state and electron structure of the materials. The XPS survey spectrum of $Ru_{4.7}/Co-Sm_2O_3$ confirmed the presence of Ru, C, O, Co and Sm signals (Fig. S6). From the high-resolution (HR) XPS spectra of C 1s + Ru 3d (Fig. 3a and Table S1), the deconvolution peaks at 284.0, 284.80, 286.0, 288.80, and 291.91 eV were identified, corresponding to C=C, C–C, C-O, C=O and π-π*, respectively, serving as calibration benchmarks [27,34]. Contemporary, the Ru $3d_{5/2}$ core level can be deconvoluted into two types of peaks at 281.40 and 283.41 eV, indexing to metallic Ru and $Ru^{\delta+}$ respectively, and confirms 54.6 % metallic Ru in $Ru/Co-Sm_2O_3$, validating successful metallic Ru preparation [35]. Owing to the extremely small particle size and large surface area of Ru, oxidation reactions inevitably occurred when exposed to air, therefore inert gas shielding during catalyst

preparation was crucial to preserve Ru's metallic phase [35]. For example, Zhang et al. prepared Ru/C catalysts on Vulcan XC-72 carriers using different methods, revealing various oxidation states of Ru [36]. High-temperature reduction and inert gas preservation could minimize Ru oxidation during catalyst preparation. The XPS peak for metallic Ru in $Ru_{4.7}/Co-Sm_2O_3$ exhibited a positive shift (0.13 eV) compared to $Ru_{4.7}/Co$, indicating a strong electron metal-support interaction in $Ru_{4.7}/Co-Sm_2O_3$ through Ru to $Co-Sm_2O_3$ electron transfer [37,38].

Regarding the Co $2p_{3/2}$ core level XPS spectrum of $Ru_{4.7}/Co-Sm_2O_3$, three distinct sub-peaks appeared at 777.55, 780.44, and 784.85 eV, matching Co^0, Co^{2+} and a satellite peak, respectively (Fig. 3b, Fig. S7a and Table S2) [39]. Furthermore, the absence of significant Co-C peaks in the C 1s XPS spectrum (Fig. S7b) proved that $Co-Sm_2O_3$ rarely formed
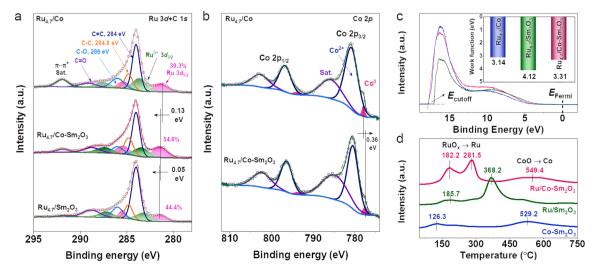

Fig. 3. High-resolution XPS of (a) C 1 s + Ru 3d, and (b) Co 2p. (c) UPS spectra with inset work functions of the different catalysts. (d) H_2-TPR profiles of $Co-Sm_2O_3$, Ru/Sm_2O_3 and $Ru/Co-Sm_2O_3$.

carbides during the high-temperature carbonization process [40]. A discernible negatively binding energy shift (0.36 eV) for Co 2p in the Ru$_{4.7}$/Co-Sm$_2$O$_3$ catalyst was observed compared with Ru$_{4.7}$/Co, highlighting the Sm species' ability to tailor the catalyst's electronic structure [41]. The HR Sm 3d spectra (Fig. S8a and Table S3) displayed two primary peaks at 1082.75 and 1110.14 eV, related to Sm 3$d_{5/2}$ and Sm 3$d_{3/2}$, respectively [42]. The consistency in Sm binding energy emphasized that Sm doping effectively orchestrates the electronic states on the catalyst's surface [24]. Moreover, the HR O 1s XPS spectrum (Fig. S8b and Table S4) of Ru$_{4.7}$/Co-Sm$_2$O$_3$ presented three peaks at 529.36, 530.91, and 531.75 eV, corresponding to metal–oxygen (M−O), carbon–oxygen (C-O/C=O), and adsorbed surface water molecules (H$_2$O$_{ads}$), respectively [43]. Collectively, these results emphasize the robust interactions between the components of the Ru$_{4.7}$/Co-Sm$_2$O$_3$ catalyst, which induces diverse electron cloud densities and thus enhances the charge carrier transport rate. Underscores the significance of charge-rich (Co-Sm$_2$O$_3$) and electron-deficient (Ru) sites in the Ru/Co-Sm$_2$O$_3$ catalyst, pivotal for BH$_4^-$ and H$_2$O adsorption/desorption, contributing to enhanced hydrolysis performance [41,44].

Ultraviolet photoelectron spectroscopy (UPS) measurements of the work function (WF) shed light on the catalysts' surface electronic attributes. The work functions for the Co, Co-Sm$_2$O$_3$, Sm$_2$O$_3$ and Ru components were 2.53, 2.66, 2.99 and 4.57 eV, respectively (Fig. S9). Differences in the WF of the catalysts indicated the transfer of electrons from higher to lower energy levels at multiphase interfaces, resulting in charge redistribution [45]. Therefore, there would be electron transfer across the interface (from Co, Co-Sm$_2$O$_3$ or Sm$_2$O$_3$ to Ru) derived from the differences of WF values, which was in agreement with the XPS analysis. Furthermore, the WFs of Ru$_{4.7}$/Co, Ru$_{4.7}$/Sm$_2$O$_3$, and Ru$_{4.7}$/Co-Sm$_2$O$_3$ were 3.14, 4.12, and 3.31 eV, respectively, as presented in Fig. 3c. We highlight that the work function of Ru$_{4.7}$/Co-Sm$_2$O$_3$ lies at an intermediate level (WF = Ru$_{4.7}$/Sm$_2$O$_3$ > Ru$_{4.7}$/Co-Sm$_2$O$_3$ > Ru$_{4.7}$/Co). This suggests the Ru$_{4.7}$/Co-Sm$_2$O$_3$ catalyst achieves a balanced capacity for electron gain and loss, effectively regulating intermediate adsorption/desorption during catalysis [46,47].

For exploration of the reduction behavior of the catalysts and the EMSI between Ru species and carriers, H$_2$ temperature-programmed reduction (H$_2$-TPR) was performed. As depicted in Fig. 3d, the Ru/Co-Sm$_2$O$_3$ showed two broad peaks at 182.2 and 281.5 °C, which were ascribed to the strong interaction of RuO$_x$ species with Co-Sm$_2$O$_3$ support and the weak interaction of RuO$_x$ species on Co-Sm$_2$O$_3$ support, respectively [48]. Notably, the reduction temperature of RuO$_x$ species in Ru/Co-Sm$_2$O$_3$ was lower than that of Ru/Sm$_2$O$_3$ (185.7 and 368.2 °C), which implied that the contact between Ru and Co-Sm$_2$O$_3$ was stronger than that between Ru and Sm$_2$O$_3$ [49]. Furthermore, a shoulder peak was observed at 126.3 °C, which was induced by oxygen adsorption [50]. Meanwhile, two broad peaks appeared at 529.2 and 549.4 °C, which may be attributed to the reduction of CoO to metallic Co [51]. The strong EMSI effect of the Ru/Co-Sm$_2$O$_3$ catalyst was favorable to promoting the rapid adsorption and desorption of the intermediate products during the hydrolysis of NaBH$_4$, accelerating the hydrogen generation rate [41].

3.4. Catalytic hydrolysis analysis

The properties of the catalysts were evaluated in a 150 mM NaBH$_4$ (with 0.4 wt% NaOH) solution at 25 °C, and the reaction setup was shown schematically in Fig. S10. According to published research, NaBH$_4$ aqueous solutions (pH = 7) undergo minor self-decomposition, as shown in Fig. S11. However, this reaction was stabilized in an alkaline environment (Fig. S12). Notably, owing to the initial catalyst wetting and pore diffusion resistance, hydrogen evolution was delayed in all samples [52]. As illustrated in Fig. 4a-b, the optimal Ru$_{4.7}$/Co-Sm$_2$O$_3$ catalyst performed the highest HGR values (HGR = 0.430 mol min^{-1} g$_{catalyst}^{-1}$), nearly 357 times that of its Co-Sm$_2$O$_3$ precursor. Concurrently, the influence of different Co/Sm molar ratios on the catalytic H$_2$ generation was investigated, finding that the HRG with Co/Sm = 30/1 was the best (Fig. 4c-d). Meanwhile, the turnover frequency (TOF) value was further calculated based on each exposed Ru atom to reflect its intrinsic catalytic activity. The Ru/Co-Sm$_2$O$_3$ catalyst yielded a TOF value of
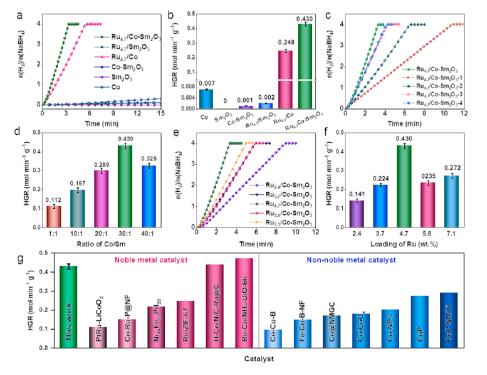

Fig. 4. (a) Relationship between the H$_2$ generation rates and reaction time of different catalysts. (b) Summarized HGR from (a). (c-d) Different Co/Sm ratios, and (e-f) different amounts of Ru. (g) Recently reported catalysts for alkaline NaBH$_4$ hydrolysis. All tests were performed in 150 mM NaBH$_4$ + 0.4 wt% NaOH solution at 25 °C.

2.39×10^4 mol_{H_2} min^{-1} mol_{Ru}^{-1} (Table S5), which was higher than those of Ru/Co (1.93×10^4 mol_{H_2} min^{-1} mol_{Ru}^{-1}) and Ru/Sm_2O_3 (2.08×10^2 mol_{H_2} min^{-1} mol_{Ru}^{-1}). Additionally, the optimal calcination temperature was fixed at 800 °C (Fig. S13). The aforementioned findings highlighted the pivotal role of Ru as a primary active site for catalyzing sodium borohydride hydrolysis, emphasizing the significance of determining the ideal Ru content. Fig. 4e-f revealed that a catalyst with a 4.7 wt% Ru content achieves the best HGR. Generally, the Ru content was positively related to the number of active sites. However, the relationship between Ru concentration and HGR follows a bell curve: while an initial increase in Ru concentration boosted HGR, further increases caused a decline. This downturn can be attributed to excessive Ru leading to agglomeration, reducing the number of active sites and HGR [10]. Comparatively, as illustrated in Fig. 4g, the HGR values of the optimized $Ru_{4.7}$/Co-Sm_2O_3 outperform most similarly reported catalysts (Table S7). In a word, the exemplary performance of $NaBH_4$ hydrolysis catalysts stemmed from a harmonious combination of an optimal support structure and the ideal Ru content, together optimizing the catalytic efficiency [12].

Given that NaOH can effectively suppresses the self-hydrolysis of $NaBH_4$, understanding its influence on HGR is essential. As delivered in Fig. 5a, varying NaOH concentrations (ranging from 0 to 0.8 wt%) did not significantly alter the HGR of the catalyzed hydrolysis. This suggested that an alkaline environment mainly stabilized $NaBH_4$, aligning with previous studies [53]. As the $NaBH_4$ concentration magnified (from 50 to 200 mM), the time for complete H_2 catalytic production extended (Fig. S14). Fig. 5b displayed that the slope value of the linear fit for ln (rate) and ln ($NaBH_4$ concentration) was 0.069, approaching to zero. The results demonstrated that the hydrolysis of $NaBH_4$ was a zero-order reaction, which can be corroborated from related reports [9]. Observing the n(H_2)/n($NaBH_4$) curves against time for $NaBH_4$ hydrolysis at temperatures from 298 to 318 K (shown in Fig. 5c and Fig. S15), the HGR notably increases with temperature. The reaction completion time dropped from 3.1 min at 298 K to just 1.0 min at 318 K. From the Arrhenius plot in Fig. 5d, the apparent activation energies (E_a) for the hydrolysis of $NaBH_4$ catalyzed by $Ru_{4.7}$/Co, $Ru_{4.7}$/Sm_2O_3 and $Ru_{4.7}$/Co-Sm_2O_3 were 45.7, 57.8 and 53.2 kJ mol^{-1}, respectively. However, hydrogen production efficiency depends on multiple factors, including

catalyst activity, component synergy, and reaction conditions, challenging direct comparisons based solely on activation energy. XPS and UPS analyses revealed a moderate electronic state for the Ru/Co-Sm_2O_3 catalyst, attributed to steric effects from interactions among Ru, Sm_2O_3, and Co vacancies, resulting in moderate kinetics of hydrogen generation [54].

In addition to the catalytic performance of $NaBH_4$ hydrolysis for hydrogen production, the recyclability of the catalyst was also an essential factor in the feasibility of large-scale applications. Over time, the HGR diminished, with the fifth cycle's HGR being 74.2 % of the initial cycle (Fig. 5e-f). An in-depth analysis of the catalyst's impressive reusability, based on its post-use morphology and surface electronic states, revealed negligible changes after five cycles (Figs. S16-S18). Nevertheless, post-reaction XPS indicates higher metallic Ru content in Ru/Co-Sm_2O_3-5th catalyst, possibly due to $Ru^{\delta+}$ reduction by $NaBH_4$ solution. Possible factors for the decline in circulatory performance were the slight flaking of the Ru particles and the possibility of some by-products (BO^{2-}) of the catalytic process (Table S6) [10].

3.5. DFT calculation and mechanism analysis

Furthermore, density functional theory (DFT) calculations were performed to investigate the potential mechanism of catalyzing $NaBH_4$ hydrolysis by Ru/Co-Sm_2O_3 catalyst. The charge difference of Ru/Co-Sm_2O_3 revealed electron accumulation at Ru edges and a lack of electrons around Co species, which was consistent with XPS results, confirming a significant electronic interaction between Ru and Co-Sm_2O_3 support (Fig. 6a). This also implied a higher electron density on Ru than on Co. Consequently, BH_4^- groups were preferentially adsorbed on the negatively charged active site, and a high molar ratio of [BH_4^-]/[Ru] facilitated electron transfer of BH_4^- ions via Ru/Co-Sm_2O_3, resulting in the desorption of H^- from BH_4^- ions. Due to the more vacant Ru 4d orbitals in Ru/Co-Sm_2O_3, the activated Ru nanoparticles can easily adsorb H^- [55]. Meanwhile, H_2O molecules tended to adsorb on hydrophilic Co-Sm_2O_3, leading to the weakening H-OH bond and promoting the dissociation of H_2O [8]. The hydrolysis mechanism of $NaBH_4$ involved two commonly used kinetic models, namely, Langmuir–Hinshelwood and Michaelis–Menten/Eley-Rideal mechanisms [56]. As shown in
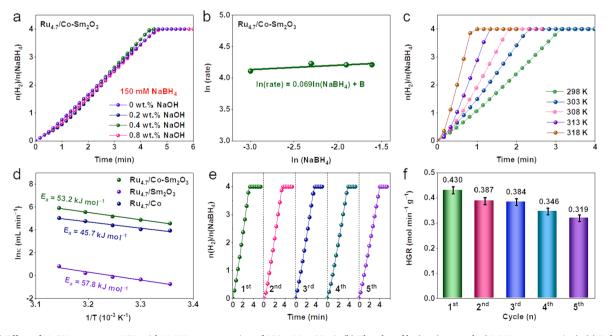

Fig. 5. (a) Effect of NaOH content on HGR with $NaBH_4$ concentration of 150 mM at 25 °C. (b) The plot of ln (rate) versus ln ($NaBH_4$ concentration). (c) Relationship between the H_2 generation rates and reaction time of different reaction temperatures (298 ~ 318 K). (d) Summarized Arrhenius diagram from (c). (e) Reusability test of $Ru_{4.7}$/Co-Sm_2O_3 catalyst at 25 °C. (f) Summarized HGR from (e). All tests were performed in 150 mM $NaBH_4$ + 0.4 wt% NaOH solution.
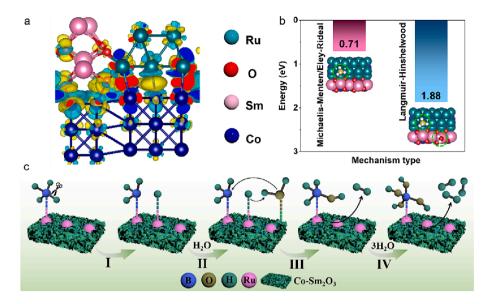
Fig. 6. (a) Charge density difference of Ru/Co-Sm$_2$O$_3$ model. (b) The energies of rate-determining steps corresponding to different mechanisms on Ru/Co-Sm$_2$O$_3$ catalyst (inset shows green circles denoting optimized adsorption points in the model). (c) Proposed catalytic mechanism schematic of Ru/Co-Sm$_2$O$_3$ catalyst for H$_2$ generation by hydrolysis of alkalized NaBH$_4$ solution. (For interpretation of the references to colour in this figure legend, the reader is referred to the web version of this article.)

Fig. 6b and Fig. S19, the rate-determining step of the Michaelis–Menten/Eley-Rideal mechanism (0.71 eV) required significantly less energy than the Langmuir-Hinshelwood mechanism (1.88 eV). Therefore, we proposed that Ru/Co-Sm$_2$O$_3$ should follow the Michaelis–Menten/Eley-Rideal mechanism to catalyze the hydrolysis of NaBH$_4$ to generate H$_2$ [57], as illustrated by the hydrolysis schematic in Fig. 6c. Specifically, the B-H bond broke firstly to produce adsorbed hydrogen (H$_{ads}$). Then, H$_{ads}$ combined with another H in the H$_2$O molecule, releasing a H$_2$ and producing BH$_3$OH. The catalytic hydrolysis reaction proceeded until the remaining H atoms in the borohydride were replaced by OH$^-$ ions and B(OH)$_4^-$ was finally dissociated [58].

4. Conclusion

Upon thorough evaluation of the provided data, we implemented a rational manipulation strategy to construct Ru$_{4.7}$/Co-Sm$_2$O$_3$ microspheres via a MOF-engaged pyrolysis-reduce method, in which Ru nanoparticles were integrated into the Co-Sm$_2$O$_3$ support, obtaining an intimately contacted superstructure. Pyrolysis treatment at 800 °C created vacancies in Ru/Co-Sm$_2$O$_3$ catalysts, which were effective in trapping and strongly coupling to Ru species, thus optimizing charge transfer and catalytically active sites. Systematic studies unveiled that the defect-induced EMSI between Ru and Co-Sm$_2$O$_3$ carriers not only achieved a controlled interface, but optimized the adsorption of intermediates species, resulting in exceptional hydrolysis performance. Specifically, the optimized Ru/Co-Sm$_2$O$_3$ exhibited superior HGR value of 0.430 mol min^{-1} g$_{catalyst}^{-1}$, along with strong cycling stability in NaBH$_4$ hydrolysis, surpassing those of its counterparts and most published catalysts. The data-driven insights presented could inform the optimization strategies for further enhancing the catalyst's performance and longevity.

CRediT authorship contribution statement

Shuqing Zhou: Writing – original draft, Methodology. **Qiuling Yang:** Validation, Investigation. **Yi Liu:** Writing – original draft, Methodology. **Lianrui Cheng:** Validation, Investigation. **Tayirjan Taylor Isimjan:** Writing – review & editing. **Jianniao Tian:** Writing – review & editing, Supervision. **Xiulin Yang:** Validation, Investigation.

Declaration of competing interest

The authors declare that they have no known competing financial interests or personal relationships that could have appeared to influence the work reported in this paper.

Data availability

Data will be made available on request.

Appendix A. Supplementary data

Supplementary data to this article can be found online at https://doi.org/10.1016/j.jcat.2024.115491.

References

[1] Q. Zhou, Z. Wang, H. Yuan, J. Wang, H. Hu, Rapid hydrogen adsorption-desorption at sulfur sites via an interstitial carbon strategy for efficient HER on MoS$_2$, Appl. Catal. B Environ. 332 (2023) 122750, https://doi.org/10.1016/j.apcatb.2023.122750.

[2] Y. Li, C. Zhuang, S. Qiu, J. Gao, Q. Zhou, Z. Sun, Z. Kang, X. Han, Cs-cu-cl perovskite quantum dots for photocatalytic H$_2$ evolution with super-high stability, Appl. Catal. B Environ. 337 (2023) 122881, https://doi.org/10.1016/j.apcatb.2023.122881.

[3] L. Ouyang, W. Chen, J. Liu, M. Felderhoff, H. Wang, M. Zhu, Enhancing the regeneration process of consumed NaBH$_4$ for hydrogen storage, Adv. Energy Mater. 7 (2017) 1700299, https://doi.org/10.1002/aenm.201700299.

[4] Y. Jing, S. Zhou, J. Liu, H. Yang, J. Liang, L. Peng, Z. Li, Y. Xia, H. Zhang, F. Xu, L. Sun, K.S. Novoselov, P. Huang, Unveiling the destabilization of sp^3 and sp^2 bonds in transition metal-modified borohydrides to improve reversible dehydrogenation and rehydrogenation, J. Colloid Interface Sci. 661 (2024) 185–195, https://doi.org/10.1016/j.jcis.2024.01.164.

[5] Y. Zhu, L. Ouyang, H. Zhong, J. Liu, H. Wang, H. Shao, Z. Huang, M. Zhu, Closing the loop for hydrogen storage: facile regeneration of NaBH$_4$ from its hydrolytic

product, Angew. Chem. Int. Ed. 59 (2020) 8623–8629, https://doi.org/10.1002/anie.201915988.

[6] J. Kirk, Y. Kim, Y.-J. Lee, M. Kim, D.-S. Min, P. Soon Kim, J. Hui Seo, Y. Kim, J. Lee, J. Woo Choung, H. Sohn, S.-W. Nam, C.-W. Yoon, Y. Kim, H. Jeong, Pushing the limits of sodium borohydride hydrolysis for on-board hydrogen generation systems, Chem. Eng. J. 466 (2023) 143233, https://doi.org/10.1016/j.cej.2023.143233.

[7] Y. Bu, J. Liu, D. Cai, P. Huang, S. Wei, X. Luo, Z. Liu, F. Xu, L. Sun, X. Wei, Magnetic recyclable catalysts with dual protection of hollow Co/N/C framework and surface carbon film for hydrogen production from NaBH₄ hydrolysis, J. Alloys Compd. 938 (2023) 168495, https://doi.org/10.1016/j.jallcom.2022.168495.

[8] C. Wu, J. Zhang, J. Guo, L. Sun, J. Ming, H. Dong, Y. Zhao, J. Tian, X. Yang, Ceria-induced strategy to tailor Pt atomic clusters on cobalt-nickel oxide and the synergetic effect for Superior hydrogen generation, ACS Sustainable Chem. Eng. 6 (2018) 7451–7457, https://doi.org/10.1021/acssuschemeng.8b00061.

[9] H. Zhang, L. Zhang, I.A. Rodríguez-Pérez, W. Miao, K. Chen, W. Wang, Y. Li, S. Han, Carbon nanospheres supported bimetallic Pt-Co as an efficient catalyst for NaBH₄ hydrolysis, Appl. Surf. Sci. 540 (2021) 148296, https://doi.org/10.1016/j.apsusc.2020.148296.

[10] J. Zhang, F. Lin, L. Yang, Z. He, X. Huang, D. Zhang, H. Dong, Ultrasmall Ru nanoparticles supported on chitin nanofibers for hydrogen production from NaBH₄ hydrolysis, Chin. Chem. Lett. 31 (2020) 2019–2022, https://doi.org/10.1016/j.cclet.2019.11.042.

[11] J. Yang, W. Li, D. Wang, Y. Li, Electronic metal-support Interaction of single-atom catalysts and applications in electrocatalysis, Adv. Mater. 32 (2020) 2003300, https://doi.org/10.1002/adma.202003300.

[12] D.D. Tuan, K.-Y.-A. Lin, Ruthenium supported on ZIF-67 as an enhanced catalyst for hydrogen generation from hydrolysis of sodium borohydride, Chem. Eng. J. 351 (2018) 48–55, https://doi.org/10.1016/j.cej.2018.06.082.

[13] L. Ding, Y. Liu, J. Lai, W. Zhu, C. Fan, N. Hao, J. Wei, J. Qian, K. Wang, Turning on high-sensitive organic electrochemical transistor-based photoelectrochemical-type sensor over modulation of Fe-MOF by PEDOT, Adv. Funct. Mater. 32 (2022) 2202735, https://doi.org/10.1002/adfm.202202735.

[14] F. Zou, Y.-M. Chen, K. Liu, Z. Yu, W. Liang, S.M. Bhaway, M. Gao, Y. Zhu, Metal organic frameworks derived Hierarchical hollow NiO/Ni/Graphene composites for lithium and sodium storage, ACS Nano 10 (2016) 377–386, https://doi.org/10.1021/acsnano.5b05041.

[15] S. Dou, W. Zhang, Y. Yang, S. Zhou, X. Rao, P. Yan, T.T. Isimjan, X. Yang, Shaggy-like ru-clusters decorated core-shell metal-organic framework-derived CoOₓ@NPC as high-efficiency catalyst for NaBH₄ hydrolysis, Int. J. Hydrogen Energy 46 (2021) 7772–7781, https://doi.org/10.1016/j.ijhydene.2020.12.011.

[16] F. Liu, Z. Fan, Defect engineering of two-dimensional materials for advanced energy conversion and storage, Chem. Soc. Rev. 52 (2023) 1723–1772, https://doi.org/10.1039/d2cs00931e.

[17] L. Shi, K. Zhu, Y. Yang, Y. Liu, S. Xu, T.T. Isimjan, X. Yang, Oxygen-vacancy-rich Ru-clusters decorated Co/Ce oxides modifying ZIF-67 nanocubes as a high-efficient catalyst for NaBH₄ hydrolysis, Int. J. Hydrogen Energy 47 (2022) 37840–37849, https://doi.org/10.1016/j.ijhydene.2022.08.289.

[18] S. Zhou, Y. Yang, W. Zhang, X. Rao, P. Yan, T.T. Isimjan, X. Yang, Structure-regulated Ru particles decorated P-vacancy-rich CoP as a highly active and durable catalyst for NaBH₄ hydrolysis, J. Colloid Interface Sci. 591 (2021) 221–228, https://doi.org/10.1016/j.jcis.2021.02.009.

[19] H. Chen, X. Yang, P. Lv, P. Tian, S. Wan, Q. Liu, Mn-doped FeS with larger lattice spacing as advance anode for sodium ion half/full battery, Chem. Eng. J. 450 (2022) 137960, https://doi.org/10.1016/j.cej.2022.137960.

[20] Y. Yang, Y. Huang, S. Zhou, Y. Liu, L. Shi, T.T. Isimjan, X. Yang, Delicate surface vacancies engineering of ru doped MOF-derived Ni-Nio@C hollow microsphere superstructure to achieve outstanding hydrogen oxidation performance, J. Energy Chem. 72 (2022) 395–404, https://doi.org/10.1016/j.jechem.2022.06.011.

[21] Y. Huang, Q. Gong, X. Song, K. Feng, K. Nie, F. Zhao, Y. Wang, M. Zeng, J. Zhong, Y. Li, Mo₂C Nanoparticles dispersed on Hierarchical Carbon microflowers for efficient electrocatalytic hydrogen evolution, ACS Nano 10 (2016) 11337–11343, https://doi.org/10.1021/acsnano.6b06580.

[22] B.C. Wu, L. Huang, L. Yan, H.Y. Gang, Y.Y. Cao, D. Wei, H.Y. Wang, Z.P. Guo, W.C. Zhang, Boron-modulated electronic-configuration tuning of cobalt for enhanced nitric oxide fixation to ammonia, Nano Lett. 23 (2023) 7120–7128, https://doi.org/10.1021/acs.nanolett.3c01994.

[23] J. Zhang, M. Cao, X. Li, Y. Xu, W. Zhao, L. Chen, Y.C. Chang, C.W. Pao, Z. Hu, X. Huang, Kinetic-modulated crystal phase of Ru for hydrogen oxidation, Small 19 (2023) 2207038, https://doi.org/10.1002/smll.202207038.

[24] J. Li, W.T. Zhong, Q. Deng, Q.M. Zhang, Z. Lin, C.H. Yang, Mechanistic origin for high structural stability of single crystalline nickel-rich cathode materials via Al and Sm co-doping, Adv. Funct. Mater. 33 (2023) 2300127, https://doi.org/10.1002/adfm.202300127.

[25] Y. Shen, L. Wang, J. Jiang, D. Wang, D. Zhang, D. Yin, L. Wang, X. Zhang, G. Huang, Y. Cheng, Stabilization of high-voltage layered oxide cathode by multi-electron rare earth oxide, Chem. Eng. J. 454 (2023) 140249, https://doi.org/10.1016/j.cej.2022.140249.

[26] Y. Liu, L. Cheng, Y. Huang, Y. Yang, X. Rao, S. Zhou, T. Taylor Isimjan, X. Yang, Electronic modulation and mechanistic study of ru-decorated porous cu-rich cuprous oxide for robust alkaline hydrogen oxidation and evolution reactions, ChemSusChem 16 (2023) e202202113.

[27] J. Li, Y. Kang, Z. Lei, P. Liu, Well-controlled 3D flower-like CoP₃/CeO₂/C heterostructures as bifunctional oxygen electrocatalysts for rechargeable zn-air batteries, Appl. Catal. B Environ. Energy 321 (2023) 122029, https://doi.org/10.1016/j.apcatb.2022.122029.

[28] D. Wang, H. Xu, P. Yang, L. Xiao, L. Du, X. Lu, R. Li, J. Zhang, M. An, A dual-template strategy to engineer hierarchically porous Fe–N–C electrocatalysts for the high-performance cathodes of Zn–air batteries, J. Mater. Chem. A 9 (2021) 9761–9770, https://doi.org/10.1039/d1ta00585e.

[29] Y. Wang, R. Gan, Z. Ai, H. Liu, C. Wei, Y. Song, M. Dirican, X. Zhang, C. Ma, J. Shi, Hollow Co₃O₄₋ₓ nanoparticles decorated N-doped porous carbon prepared by one-step pyrolysis as an efficient ORR electrocatalyst for rechargeable zn-air batteries, Carbon 181 (2021) 87–98, https://doi.org/10.1016/j.carbon.2021.05.016.

[30] Z. Deng, C. Ma, Z. Li, Y. Luo, L. Zhang, S. Sun, Q. Liu, J. Du, Q. Lu, B. Zheng, X. Sun, High-efficiency electrochemical nitrate reduction to ammonia on a Co₃O₄ Nanoarray catalyst with cobalt vacancies, ACS Appl. Mater. Interfaces 14 (2022) 46595–46602, https://doi.org/10.1021/acsami.2c12772.

[31] S. Jiang, R. Zhang, H. Liu, Y. Rao, Y. Yu, S. Chen, Q. Yue, Y. Zhang, Y. Kang, Promoting formation of oxygen vacancies in two-dimensional cobalt-doped ceria nanosheets for efficient oxygen evolution, J. Am. Chem. Soc. 142 (2020) 6461–6466, https://doi.org/10.1021/jacs.9b13915.

[32] X. Lei, J. Wang, T. Wang, X. Wang, X. Xie, H. Huang, D. Li, Z. Ao, Toluene decomposition by non-thermal plasma assisted CoOx−γ-Al2O3: the relative contributions of specific energy input of plasma, Co3+ and oxygen vacancy, J. Hazard. Mater. 456 (2023) 131613, https://doi.org/10.1016/j.jhazmat.2023.131613.

[33] L. Gong, H. Zhang, Y. Wang, E. Luo, K. Li, L. Gao, Y. Wang, Z. Wu, Z. Jin, J. Ge, Z. Jiang, C. Liu, W. Xing, Bridge bonded oxygen ligands between approximated FeN₄ sites confer catalysts with high ORR performance, Angew. Chem. Int. Ed. 59 (2020) 13923–13928, https://doi.org/10.1002/anie.202004534.

[34] Y. Liu, Y. Huang, S. Zhou, Y. Yang, L. Cheng, T.T. Isimjan, X. Yang, Synergistic regulation of Pt clusters on porous support by Mo and P for robust bifunctional hydrogen electrocatalysis, Inorg. Chem. 62 (2023) 8719–8728, https://doi.org/10.1021/acs.inorgchem.3c01017.

[35] Y. Liu, X. Li, Q. Zhang, W. Li, Y. Xie, H. Liu, L. Shang, Z. Liu, Z. Chen, L. Gu, Z. Tang, T. Zhang, S. Lu, A general route to Prepare low-ruthenium-content Bimetallic electrocatalysts for pH-universal hydrogen evolution reaction by using Carbon quantum dots, Angew Chem. Int. Ed. 59 (2020) 1718–1726, https://doi.org/10.1002/anie.201913910.

[36] Z. Li, L. An, M. Song, T. Zhao, J. Zhang, C. Zhang, Z. Li, D. Wang, Tuning the hydrogen and hydroxyl adsorption on Ru nanoparticles for hydrogen electrode reactions via size controlling, Chin. Chem. Lett. 34 (2023) 107622, https://doi.org/10.1016/j.cclet.2022.06.045.

[37] Y. Liu, Y. Zou, Y. Wang, Y. Ma, S. Zhang, Y. Qu, Strong metal-support interactions between Pt and CeO₂ for efficient methanol decomposition, Chem. Eng. J. 475 (2023) 146219, https://doi.org/10.1016/j.cej.2023.146219.

[38] Q. Huang, P. Huang, Z. Sun, Y. Zhang, Y. Xia, H. Peng, Y. Zou, H. Chu, E. Yan, F. Xu, L. Sun, De-hybridization effect of transition metal catalysts on AlH₄-based hydrogen storage materials, Physica B: Condensed Matter 623 (2021) 413343, https://doi.org/10.1016/j.physb.2021.413343.

[39] Q. Liu, J. Huang, H. Tang, X. Yu, J. Shen, Construction 0D TiO₂ nanoparticles/2D CoP nanosheets heterojunctions for enhanced photocatalytic H₂ evolution activity, J. Mater. Sci. Technol. 56 (2020) 196–205, https://doi.org/10.1016/j.jmst.2020.04.026.

[40] Z. Yang, T. Zhao, S. Hao, R. Wang, C. Zhu, Y. Tang, C. Guo, J. Liu, X. Wen, F. Wang, Large-scale synthesis of multifunctional single-phase Co2C nanomaterials, Adv. Sci. 10 (2023) 2301073, https://doi.org/10.1002/advs.202301073.

[41] S. Zhou, L. Cheng, Y. Huang, Y. Liu, L. Shi, T.T. Isimjan, X. Yang, Constructing Ru particles decorated Co₃B-CoP heterostructures as a highly active and reusable catalyst for H₂ generation by catalyzing NaBH₄ hydrolysis, Appl. Catal. B Environ. 328 (2023) 122519, https://doi.org/10.1016/j.apcatb.2023.122519.

[42] M.R. Kosinski, A.J. Vizcaíno, L.M. Gómez-Sainero, A. Carrero, R.T. Baker, Methanol reforming by nanostructured Pd/Sm-doped ceria catalysts, Appl. Catal. B Environ. 286 (2021) 119935, https://doi.org/10.1016/j.apcatb.2021.119935.

[43] W. Liang, M. Zhou, X. Lin, J. Xu, P. Dong, Z. Le, M. Yang, J. Chen, F. Xie, N. Wang, Y. Jin, H. Meng, Nickel-doped tungsten oxide promotes stable and efficient hydrogen evolution in seawater, Appl. Catal. B Environ. 325 (2023) 122397, https://doi.org/10.1016/j.apcatb.2023.122397.

[44] X. Cao, J. Zhou, Z. Zhai, S. Li, G. Yuan, G. Qin, Synchronous growth of porous MgO and half-embedded Nano-Ru on a Mg plate: a monolithic catalyst for fast hydrogen production, ACS Sustain. Chem. Eng. 9 (2021) 3616–3623, https://doi.org/10.1021/acssuschemeng.1c00072.

[45] Y. Li, C. Yang, J. Yue, H. Cong, W. Luo, Polymorphism-Interface-induced work function regulating on Ru nanocatalyst for enhanced alkaline hydrogen oxidation reaction, Adv. Funct. Mater. 33 (2023) 2211586, https://doi.org/10.1002/adfm.202211586.

[46] L. Su, X. Fan, Y. Jin, H. Cong, W. Luo, Hydroxyl-binding energy-induced kinetic gap Narrowing between acidic and alkaline hydrogen oxidation reaction on Intermetallic Ru₃Sn₇ catalyst, Small 19 (2023) 2207603, https://doi.org/10.1002/smll.202207603.

[47] A.P. Baddorf, A.J. Rondinone, D.K. Hensley, Work function measurements of clean and modified carbon nanospikes, Carbon 168 (2020) 302–307, https://doi.org/10.1016/j.carbon.2020.06.072.

[48] Y. Guo, S. Mei, K. Yuan, D.-J. Wang, H.-C. Liu, C.-H. Yan, Y.-W. Zhang, Low-temperature CO₂ methanation over CeO₂-supported ru single atoms, nanoclusters, and nanoparticles competitively tuned by strong metal-support interactions and H-spillover effect, ACS Catal. 8 (2018) 6203–6215, https://doi.org/10.1021/acscatal.7b04469.

[49] G.D. Sun, Z.J. Zhao, R.T. Mu, S.J. Zha, L.L. Li, S. Chen, K.T. Zang, J. Luo, Z.L. Li, S.C. Purdy, A.J. Kropf, J.T. Miller, L. Zeng, J.L. Gong, Breaking the scaling relationship via thermally stable Pt/Cu single atom alloys for catalytic

dehydrogenation, Nat. Commun. 9 (2018) 4454, https://doi.org/10.1038/s41467-018-06967-8.

[50] H. Huang, Q. Dai, X. Wang, Morphology effect of Ru/CeO_2 catalysts for the catalytic combustion of chlorobenzene, Appl. Catal. B Environ. 158–159 (2014) 96–105, https://doi.org/10.1016/j.apcatb.2014.01.062.

[51] Y. Tang, T. Zhao, H. Han, Z. Yang, J. Liu, X. Wen, F. Wang, Ir-CoO active centers supported on porous Al2O3 nanosheets as efficient and durable photo-thermal catalysts for CO2 conversion, Adv. Sci. 10 (2023) 2300122, https://doi.org/10.1002/advs.202300122.

[52] J. Li, X. Hong, Y. Wang, Y. Luo, P. Huang, B. Li, K. Zhang, Y. Zou, L. Sun, F. Xu, F. Rosei, S.P. Verevkin, A.A. Pimerzin, Encapsulated cobalt nanoparticles as a recoverable catalyst for the hydrolysis of sodium borohydride, Energy Storage Mater. 27 (2020) 187–197, https://doi.org/10.1016/j.ensm.2020.01.011.

[53] R. Fernandes, N. Patel, A. Miotello, Hydrogen generation by hydrolysis of alkaline $NaBH_4$ solution with Cr-promoted Co–B amorphous catalyst, Appl. Catal. B Environ. 92 (2009) 68–74, https://doi.org/10.1016/j.apcatb.2009.07.019.

[54] A. Guan, Q. Wang, Y. Ji, S. Li, C. Yang, L. Qian, L. Zhang, L. Wu, G. Zheng, Steric effect induces CO electroreduction to CH_4 on Cu–Au alloys, J. Mate. Chem. A 9 (2021) 21779–21784, https://doi.org/10.1039/d1ta06162c.

[55] T.-F. Hung, H.-C. Kuo, C.-W. Tsai, H.M. Chen, R.-S. Liu, B.-J. Weng, J.-F. Lee, An alternative cobalt oxide-supported platinum catalyst for efficient hydrolysis of sodium borohydride, J. Mater. Chem. 21 (2011) 11754, https://doi.org/10.1039/c1jm11720c.

[56] U.B. Demirci, P. Miele, Reaction mechanisms of the hydrolysis of sodium borohydride: a discussion focusing on cobalt-based catalysts, C. r. Chimie 17 (2014) 707–716, https://doi.org/10.1016/j.crci.2014.01.012.

[57] H. Li, X. Hu, L. Wang, L. Shi, T.T. Isimjan, X. Yang, Kinetically promoted hydrogen generation by ru nanoparticles decorated CoB_2O_4 on mesoporous carbon spheres with rich oxygen vacancies for $NaBH_4$ hydrolysis, Chem. Eng. J. 481 (2024) 148547, https://doi.org/10.1016/j.cej.2024.148547.

[58] J. Ji, K. Deng, J. Li, Z. Zhang, X. Duan, H. Huang, In situ transformation of 3D Co_3O_4 nanoparticles to 2D nanosheets with rich surface oxygen vacancies to boost hydrogen generation from $NaBH_4$, Chem. Eng. J. 424 (2021) 130350, https://doi.org/10.1016/j.cej.2021.130350.